

Lithospheric structure of the Chinese mainland determined from joint inversion of regional and teleseismic Rayleigh-wave group velocities

Mei Feng¹ and Meijian An¹

Received 7 May 2008; revised 27 October 2009; accepted 15 January 2010; published 24 June 2010.

[1] We processed a large number of vertical-component seismograms recorded by broadband seismic stations in and around China and ultimately retrieved ~33 140 regional and ~10 360 teleseismic fundamental-mode group-velocity measurements at 40 s periods, with fewer measurements for shorter and longer periods. We directly inverted the processed group-velocity measurements for a three-dimensional lithospheric *S*-velocity model of the Chinese mainland. Synthetic test results and data fit or misfit analysis demonstrated the reliability of our surface-wave tomographic inversion. The imaged upper-crustal low velocities are consistent with variations in sediment thickness; for example, the Tarim Basin, which contains a great thickness of sediments, is characterized by a strong, shallow, low-velocity anomaly. High lithospheric velocities are observed to varying depths in the North China Craton, Yangtze Craton, and Tarim Craton, indicating varying thicknesses of the lithosphere beneath these cratonic areas. Low asthenospheric velocities are widely imaged in eastern and southern China, around the Tarim Basin, and along a roughly north-south belt in central China. The low asthenospheric velocities in eastern and southern China are attributed to partial melting of a subducted slab associated with the westward subduction of an oceanic plate, while those in central China and around the Tarim Basin are attributed to Indian-Eurasian collision.

Citation: Feng, M., and M. An (2010), Lithospheric structure of the Chinese mainland determined from joint inversion of regional and teleseismic Rayleigh-wave group velocities, *J. Geophys. Res.*, 115, B06317, doi:10.1029/2008JB005787.

1. Introduction

[2] The Chinese mainland, the eastern portion of the Eurasian continent, is a tectonically complex region consisting of Precambrian platforms/cratons, Phanerozoic tectonic domains, and sedimentary basins (Figure 1). The Precambrian cratonic regions include the Tarim Craton in northwestern China, the Yangtze Craton in the center, and the North China Craton (NCC) (also known as the Sino-Korean Craton) in the north. The Phanerozoic tectonic domains include the Tethyan Domain in the west and southwest of China (active since ~250 Ma), the Paleo-Asian Domain in the north and northwest (active until ~260 Ma), and the Circum-Pacific Domain in the east (active since ~250 Ma). Most of the sedimentary basins in China are intracratonic, including the Tarim Basin in the Tarim Craton, the Sichuan Basin in the Yangtze Craton, and the Ordos and Bohai Bay basins in the NCC [Ren *et al.*, 1999].

[3] The Chinese mainland has been affected by several tectonic events since the late Mesozoic. The well-known collision between the Indian and the Eurasian plates

occurred at ~50 Ma, following cessation of Tethyan subduction beneath the Eurasian continent. Indian-Eurasian collision has strongly influenced the Chinese mainland including the strongly uplifted Qinghai-Tibetan Plateau. Consistent with isostatic compensation theory, the crust of the Qinghai-Tibetan Plateau is up to ~70 km thick, and the lithospheric upper mantle appears to be double its usual thickness. However, relatively little is known regarding areas of extension and the mechanism by which collision has influenced the Chinese mainland. For example, the Tarim Craton, located on the northwest margin of the Qinghai-Tibetan Plateau, appears to be unaffected by the Indian-Eurasian collision or Tethyan subduction, as the crust in the craton is cold and stable. In addition, the Qiangtang Terrane appears to be only weakly deformed by the Indian-Eurasian collision compared with surrounding areas, as the lithospheric upper mantle in this terrane is hot and of normal thickness (i.e., not doubled in thickness).

[4] The contemporary tectonic framework and geographic relief of the Chinese mainland reflect not only collision with the Indian Plate to the southwest but also subduction of the Pacific and Philippine oceanic plates to the east. Unlike most old and stable cratons throughout the world [Artemieva and Mooney, 2001] (e.g., the Sao Francisco Craton in South America [Schimmel *et al.*, 2003] and the North American Craton [Goes and Van der Lee, 2002]), which are unaffected

¹Institute of Geomechanics, Chinese Academy of Geological Sciences, Beijing, China.

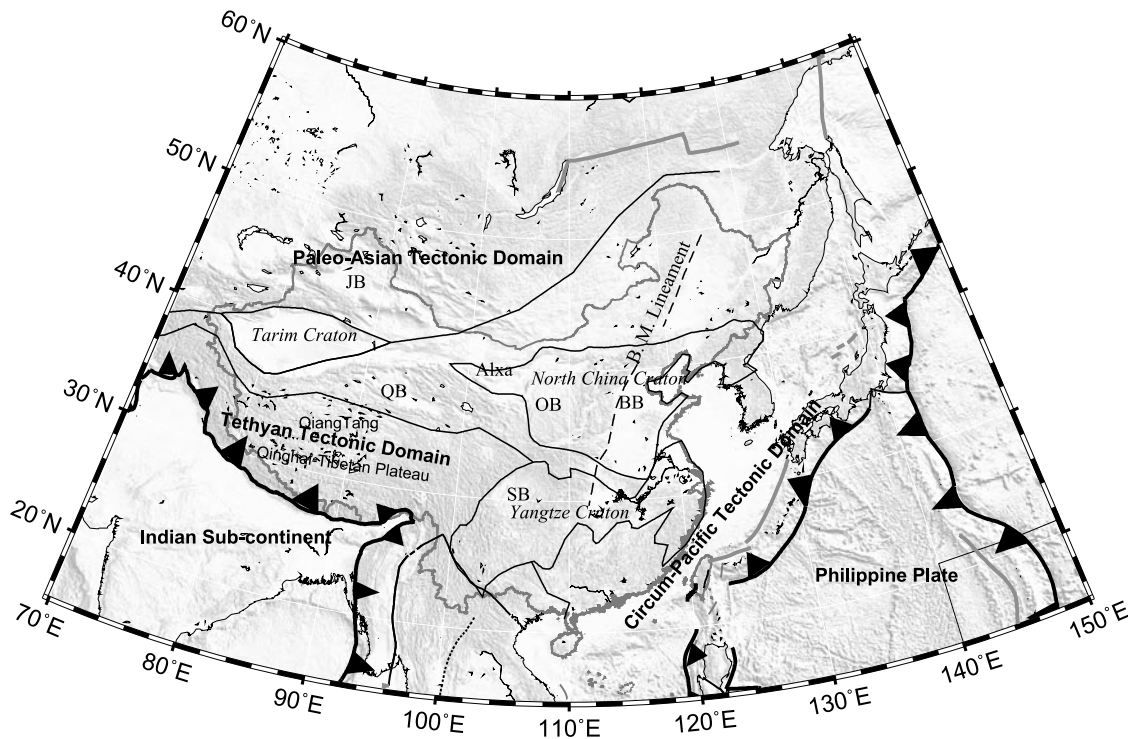


Figure 1. Simplified geotectonic map of China, shaded based on topography gradient. The B.M. Lineament is the NE-SW-trending lineament that marks the basin-mountain transition in eastern China. Tectonic boundaries are after Ren *et al.* [1999]. Plate boundaries, such as trenches and underthrusting zones (bold lines with arrowheads), spreading ridges (thick gray lines), and transform faults (thin gray lines), are from the Web site <http://www.ig.utexas.edu/research/projects/plates>. JB, Junggar Basin; QB, Qaidam Basin; OB, Ordos Basin; BB, Bohai Bay Basin; SB, Sichuan Basin.

by recent tectonic movements and have a thick lithosphere (>200 km), the cratonic regions in China covered by Archean crust record tectonic reworking and are characterized by a relatively thin lithosphere. For example, the NCC has a very thin lithosphere (~ 80 km) [An and Shi, 2006]. The nature of the processes that produced the thin, weak lithosphere within Chinese cratons, especially for the NCC, remains debated [e.g., Menzies *et al.*, 2007; Zhai *et al.*, 2007].

[5] To better understand the complex dynamical mechanisms and unique evolution history of the Chinese mainland, many geoscientists have explored its two-dimensional (2-D) and three-dimensional (3-D) seismic structure using various seismic tomography methods [Bijwaard *et al.*, 1998; Bijwaard and Spakman, 2000; Feng and An, 2007; Feng and Teng, 1983; Friederich, 2003; He *et al.*, 2002; Huang and Zhao, 2006; Huang *et al.*, 2003; Lebedev and Nolet, 2003; Li *et al.*, 2006; Liu *et al.*, 1989, 1991; Ritzwoller and Levshin, 1998; Song *et al.*, 1994; van der Voo *et al.*, 1999; Wu and Levshin, 1994; Yanovskaya and Kozhevnikov, 2003; Zhang, 1998; Zhu *et al.*, 2002]. These previous studies generally reported similar regional-scale features, such as the thick crust and double-thickness lithosphere beneath the Qinghai-Tibetan Plateau, the thin lithosphere beneath the NCC, and a relatively shallow cratonic root beneath the ancient Yangtze Craton compared with other stable cratons of comparable

age throughout the world. Despite these similarities, there exist local-scale inconsistencies among the various models, especially for the less-studied western China, possibly because of the contrasting methods and data sets employed in the various studies.

[6] It is well known that teleseismic body-wave tomography contributes little to constraining the shallow crustal and lithospheric structures because of quasi-vertically incident rays. Surface-wave tomography is an efficient and reliable approach to retrieving lithospheric S -velocity structures. For example, Huang *et al.* [2003] inverted ~ 4000 Rayleigh-wave group-velocity dispersions in constructing a lithospheric S -velocity model of the Chinese mainland. This model was further analyzed by An and Shi [2006], who derived useful seismic-thermal information for the Chinese mainland. However, in terms of surface-wave tomography, improved data coverage would produce superior resolved results. Therefore, the aim of the present study was to derive an independent 3-D lithospheric S -velocity model for the Chinese mainland using a large number of group-velocity measurements.

2. Data and Processing

[7] The present study is based on observations of fundamental-mode Rayleigh-wave group-velocity dispersion. The employed tomographic inversion method (as described

in the following section) enables the use of both regional (i.e., with entire paths within the study region) and teleseismic (i.e., with epicenters or stations located outside the study region) group-velocity measurements. Accordingly, we collected a large number of vertical-component seismograms recorded by 283 seismic stations deployed in and around China. Among these stations, 91 are part of six permanent networks (China Regional Seismograph Network, New China Digital Seismograph Network, Broadband Array in Taiwan, Global Seismograph Network, Geoscope, and Kazakhstan Network), and the other 192 stations are from seven temporary seismic networks or arrays (North China Experiment, 2000–2001; Bhutan, 2002–2003; Tibetan Plateau Broadband Experiment, 1991–1992; NE China Seismic Experiment, 1998–1999; INDEPTH III, 1998–1999; Tien Shan Continental Dynamics, 1998–2000; and Himalayan Nepal Tibet Experiment, 2001–2002).

[8] The seismic stations and events used in this study are shown in Figure 2a as triangles and circles, respectively. The inclusion of stations from the China Regional Seismograph Network and from temporary networks greatly improves the path coverage density (Figure 2) and will hopefully result in a better resolved crustal and lithospheric S -velocity model for China. The path density shown in Figure 2 is defined as the number of measurements intersecting each $1^\circ \times 1^\circ$ ($\sim 10,000$ km²) cell. Regions within the Chinese mainland have a coverage density of better than 200 rays at a 30 s period and better than 150 rays at a 120 s period.

[9] The period range of each dispersion curve depends on the magnitude of the earthquake and path length: longer periods generated by larger earthquakes are better recorded at greater epicentral distances. Figure 3 shows the total number of observations and average epicentral distances for different periods, where solid lines represent regional group-velocity measurements with rays completely within the study region, and dashed lines represent teleseismic group-velocity measurements with epicenters located outside the study region. The numbers of measurements for short periods (<30 s) and long periods (>120 s) are smaller than those for intermediate periods (30–120 s), and the numbers of regional and teleseismic group-velocity measurements for the 40 s period are $\sim 33,140$ and $\sim 10,360$, respectively, much larger than the number (~ 4000) used in the work of *Huang et al.* [2003]. The average epicenter distance for regional group-velocity measurements is $\sim 13^\circ$ (~ 1400 km) for a period of 10 s, shorter than the 2400 km (at the same period) used in the work of *Huang et al.* [2003].

[10] Rayleigh-wave group velocities are processed using a multiple filtering technique (MFT) [*Dziewonski et al.*, 1969] with the aid of the frequency-time analysis software [*Herrmann and Ammon*, 2002]. Several regular data processing steps, such as band-pass filtering, instrument response correction, and higher-mode elimination by phase-matched filtering, are employed to improve dispersion quality. A detailed description of dispersion processing with the multiple filtering technique is given in the works of *Feng et al.* [2004] and *Feng and An* [2007]. Finally, processed dispersions with instantaneous periods are spline-interpolated. Epicenters and event-origin-time data, as

required by group-velocity calculations, are taken from the Engdahl-Hilst-Buland (EHB) catalog [*Engdahl et al.*, 1998].

3. Surface-Wave Inversion for Three-Dimensional S -Velocity Structure

[11] Surface-wave dispersion is nonlinearly related to S velocities beneath the raypath of the surface wave. The linearized method [e.g., *Herrmann*, 1987] and the global random optimization algorithm [e.g., *An and Assumpção*, 2006; *Lomax and Snieder*, 1995; *Martnez et al.*, 2000; *Shapiro and Ritzwoller*, 2002; *Snoke and Sambridge*, 2002] have been widely applied in dispersion inversions. The global algorithm is superior to the linearized method in that it can sample a wide model space and yield an ensemble of acceptable models, thereby enabling better model appraisal; however, its inefficiency and simple model parameterization (i.e., a restricted number of unknowns) prevent its application in 3-D tomographic studies. Moreover, *An and Assumpção* [2006] showed that solutions obtained using linearized inversion [*Snoke and James*, 1997] are negligibly different from those obtained using global algorithms [*An and Assumpção*, 2006; *Snoke and Sambridge*, 2002]. The linearized method has been widely used in surface-wave dispersion inversion from large-scale seismic lithospheric studies [e.g., *Di Luccio and Pasyanos*, 2007; *Feng et al.*, 2004; *Herrmann*, 1987; *Huang et al.*, 2003; *Rapine et al.*, 2003] to local-scale studies, such as the detection of shallow soil structure in earthquake engineering [e.g., *Xia et al.*, 1999; *Zomorodian and Hunaidi*, 2006]. For this reason, we employed equations of the linearized approximation in our surface-wave tomographic inversion.

[12] Diffraction tomography using spatially extended finite-frequency sensitivity kernels is theoretically superior to conventional ray-theory surface-wave tomography. However, global tomography studies have shown that, in most continental regions, diffraction tomography and ray-theory tomography recover similar structure for periods shorter than 50 s [*Ritzwoller et al.*, 2002] and that a regional ray-theory tomography with dense path coverage and certain inversion regularization yields results nearly identical to those obtained when considering the finite-frequency effect [*Sieminski et al.*, 2004]. With the ongoing deployment of broadband seismic stations worldwide, the marked improvements in seismic path coverage mean that there is now little difference between the results of ray-theory tomography and those of diffraction tomography. Here the surface-wave tomography is based on ray theory.

[13] In most previous surface-wave tomography studies, inversions of dispersion measurements for a 3-D S -velocity model have been partitioned into two main steps: period-by-period 2-D tomographic inversions for regionalized dispersions and cell-by-cell inversions of regionalized dispersions for 1-D S -velocity profiles [*Feng et al.*, 2004; *Huang et al.*, 2003; *Ritzwoller and Levshin*, 1998; *Ritzwoller et al.*, 2002; *Villaseñor et al.*, 2001]. Using the partitioned method, regional group or phase velocities and 3-D S velocities have been successfully imaged for many different regions. However, this approach is inconvenient for a posteriori model appraisal because many separate forward/inversion

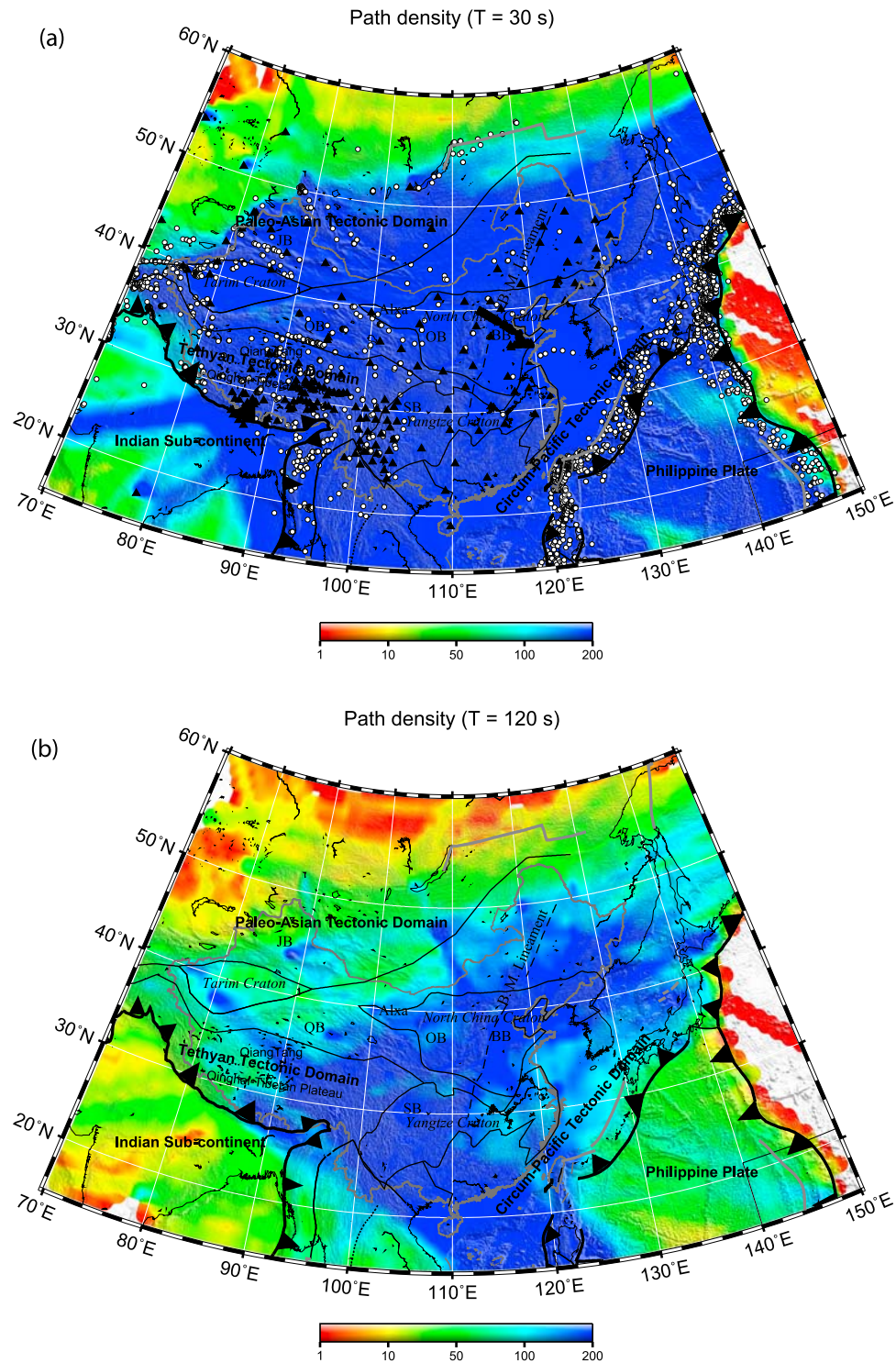


Figure 2. Path density for periods of (a) 30 s and (b) 120 s. Triangles and circles in Figure 2a are seismic stations and epicenters within the study region, respectively. The other symbols and abbreviations are as in the caption to Figure 1.

calculations are required for both the period-by-period group-velocity tomographic inversions in the first step and the cell-by-cell 1-D S -velocity profile inversions in the second step.

[14] In the present study, based on the same physical concept as that used in the traditional two-step inversion

method, we combined the two-step inversion equations into one formulation to directly invert surface-wave dispersion measurements for a 3-D S -velocity model. The modified surface-wave tomographic method requires the pre-definition of 3-D grids formed by 2-D cells in the x and y directions and 1-D homogenous layers in the z direction.

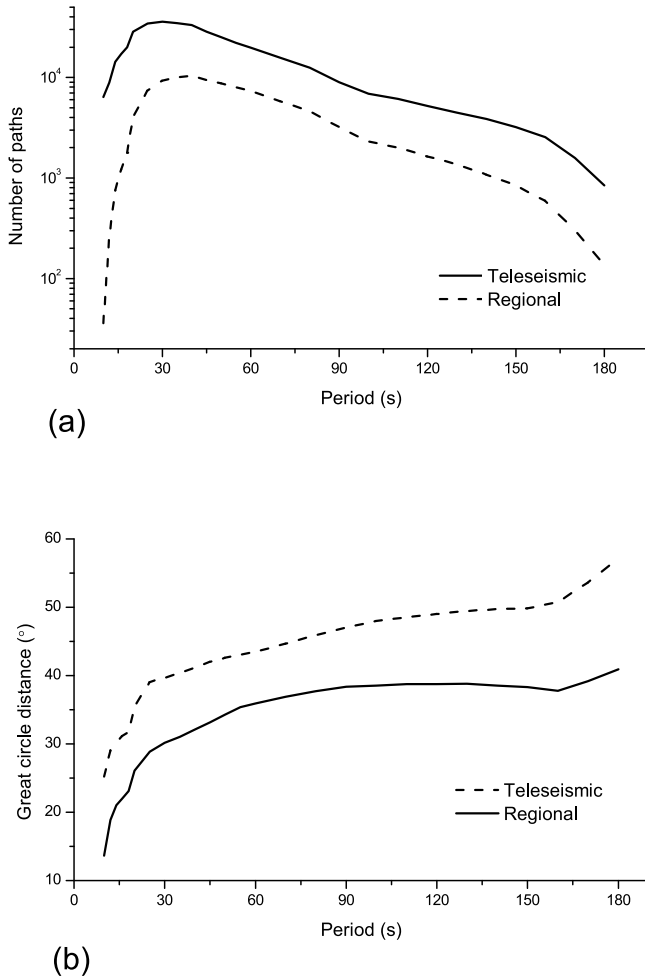


Figure 3. Observational data showing (a) the number of observational dispersions and (b) the average epicentral distance for different periods. Solid lines (regional) represent rays completely within the study region, and dashed lines (teleseismic) represent rays with epicenters located outside the study region but with stations located within the study region.

[15] For a regional raypath (m th) with both epicenters and stations located within the study region, the travel time t_m for the path can be expressed as the path length L_m divided by the group velocity U_m of a certain period:

$$t_m = \frac{L_m}{U_m} = \sum_{i=1}^{nxy} l_i s_i, \quad (1)$$

where l_i and s_i are the ray segment and group slowness (reciprocal of group velocity) in the i th horizontal cell, respectively, and nxy is the total number of cells. The surface-wave slowness in the i th cell ($s_i = s_0 + \Delta s_i$) can be considered as the sum of the slowness of the reference model s_0 and a slowness perturbation Δs_i . Substituting s_i into equation (1), we obtain

$$t_m = \sum_{i=1}^{nxy} l_i (s_0 + \Delta s_i), \quad (2)$$

where the slowness perturbation Δs_i is related to the reference model's S velocities (β) in the following first-order (linearized) approximation:

$$\Delta s_i = \sum_{j=1}^{nz} \left(\frac{\partial s_0}{\partial \beta_{ij}} \Delta \beta_{ij} \right), \quad (3)$$

where $\partial s_0 / \partial \beta_{ij}$ is the partial derivative of the group slowness to the reference S velocity, $\Delta \beta_{ij}$ is the S -velocity perturbation relative to the reference model for the grid located on the j th layer beneath the i th cell, and nz is the total number of vertical layers in each cell. Substituting equation (3) into equation (2), we obtain

$$t_m = \sum_{i=1}^{nxy} l_i \left(s_0 + \sum_{j=1}^{nz} \frac{\partial s_0}{\partial \beta_{ij}} \Delta \beta_{ij} \right); \quad (4)$$

subsequently, equation (4) can be written as

$$\sum_{i=1}^{nxy} \sum_{j=1}^{nz} \left(l_i \frac{\partial s_0}{\partial \beta_{ij}} \Delta \beta_{ij} \right) = t_m - \sum_{i=1}^{nxy} l_i s_0, \quad (5)$$

where, except for the S -velocity perturbations ($\Delta \beta_{ij}$), all other parameters are known. Therefore, resolving $\Delta \beta_{ij}$ from equation (5) is a linear inverse problem. Equation (5) only represents a linear constraint for one period in one surface-wave dispersion. By collecting many dispersions over more periods, we can obtain a large number of linear equations similar to equation (5). The compact form for many such equations can be expressed as

$$\mathbf{G}_{in} \cdot \mathbf{x} = \mathbf{t}_{in}, \quad (6)$$

where \mathbf{G}_{in} is the large-sparse coefficient matrix for rays with both events and stations located within the study region, \mathbf{x} is the vector of unknowns ($\Delta \beta_{ij}$) to be determined, and \mathbf{t}_{in} is the vector of constants from group-velocity measurements.

[16] In the preceding introduction, only regional observations with both events and stations located within the study region are considered; however, given a slightly modified equation, it is also possible to use teleseismic observations for stations or events located outside the study region. For teleseismic observations with either epicenters or stations located outside the study region, it is not possible to use the measured group velocities directly. Figure 4 shows a schematic illustration for two close paths from an epicenter located outside the study area. If path OK is close enough to path OP so that the distance AB along the wavefront is less than one wavelength, OA and OB can then be supposed to have same structure. In this case, for the m th pair of close paths (e.g., k th and p th paths in Figure 4), the travel-time difference Δt_m between the two close paths can be taken as being mainly contributed by the parts (AK and BP) located within the study region. It can then be expressed as

$$\Delta t_m = \frac{L_k}{U_k} - \frac{L_p}{U_p} = \left(L_{OA} s_{OA} + \sum_{i=1}^{nxy} l_i^{AK} s_i \right) - \left(L_{OB} s_{OB} + \sum_{i=1}^{nxy} l_i^{BP} s_i \right), \quad (7)$$

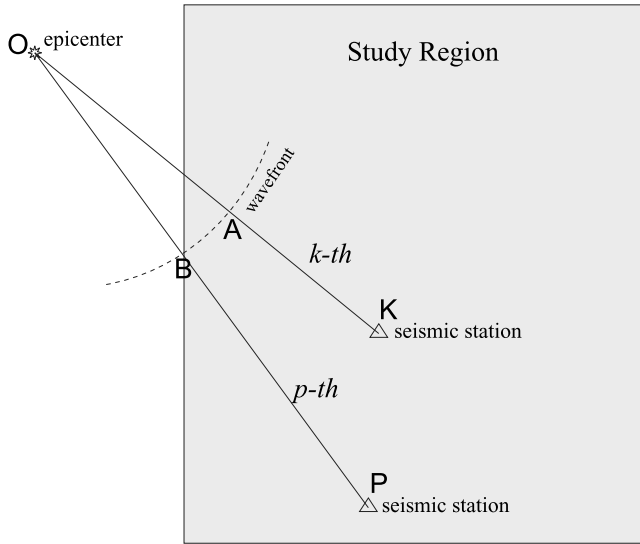


Figure 4. Geometry of two close raypaths located partly within the study region.

where the parameters are as defined in equation (1). Because OA and OB can be considered as the same structure ($s_{OA} = s_{OB}$ and $L_{OA} = L_{OB}$), equation (7) becomes

$$\Delta t_m = \sum_{i=1}^{nxy} (l_i^{AK} - l_i^{BP}) s_i. \quad (8)$$

Equation (8) is similar to equation (1), although travel time becomes travel-time difference, and ray segment becomes ray-segment difference. Transforming equation (8) by following the same steps employed from equations (2) to (5), we obtain

$$\sum_{i=1}^{nxy} \sum_{j=1}^{nz} \left[(l_i^{AK} - l_i^{BP}) \frac{\partial s_0}{\partial \beta_{ij}} \right] \Delta \beta_{ij} = \Delta t_m - \sum_{i=1}^{nxy} (l_i^{AK} - l_i^{BP}) s_0, \quad (9)$$

where again, except for $\Delta \beta_{ij}$, all the parameters are known. Therefore, resolving $\Delta \beta_{ij}$ is a linear inverse problem. Combining all the constraints from such close-path pairs, we obtain

$$\mathbf{G}_{out} \cdot \mathbf{x} = \mathbf{t}_{out}. \quad (10)$$

Because both \mathbf{G}_{in} and \mathbf{G}_{out} are large and sparse matrices, a priori constraints are required to regularize the inversion. Here we introduce 3-D smoothing as the a priori constraints (\mathbf{S}) to produce a more physically reasonable model. The 3-D smoothing constraints suppose that each neighboring pair of parameters in the x , y , or z direction has similar physical properties (i.e., their difference tends to be 0). For the traditional two-step method, neighboring parameters can only be considered in the x and y directions in the first step and in the z direction in the second step. Consequently, the final 3-D model cannot be simultaneously smoothed laterally (x and y directions) and vertically (z direction). By combining the constraints for raypaths both within and

partly within the study region and the 3-D smoothing constraints, we obtain

$$\begin{pmatrix} \mathbf{G}_{in} \\ \mathbf{G}_{out} \\ \lambda \mathbf{S} \end{pmatrix} \mathbf{x} = \begin{pmatrix} \mathbf{t}_{in} \\ \mathbf{t}_{out} \\ \mathbf{0} \end{pmatrix}, \quad (11)$$

where λ is a weighting factor to balance between fitting the data and smoothing the model. We use the program LSQR [Paige and Saunders, 1982a, 1982b] to resolve \mathbf{x} from equation (11).

[17] In a linearized inversion, multiple iterations are normally required to approximate the real solution, step by step. Therefore, it would seem necessary also to run the 3-D inversion iteratively. Figure 5 shows the results of synthetic tests over several iterations, using simple reference models. Subsequent iterations (fourth and fifth columns) do show some minor improvement in the recovery of the true model structures compared with the first iteration, but despite the large difference between the true model (first column) and the reference model (second column), the model of the first iteration (third column) reliably recovers most of the structures of the true model, except for those around the discontinuity (reflecting the inherent trade-off between S velocities and discontinuity depth). Therefore, our one-step 3-D surface-wave inversion method is able to retrieve the first-order major structures after only one run of inversion.

[18] It seems difficult to understand why the 3-D inversion almost converges after only a single run. A possible explanation is that our sensitivity matrix \mathbf{G} occurs in three dimensions, consisting of not only a vertical component of linearized partial derivatives, but also a lateral component of linear ray-propagation constraints. Iterative runs are important for linearized inversion but unnecessary for a linear inversion. Therefore, it is a reasonable result that further iterations produce minor improvement in the solution of our inversion combined with linearized and linear inverse problems. In addition, the structure recovery of the first iteration, using two quite different reference models (Figures 5a and 5b), is reasonably good, thereby suggesting that our combined formulation is able to reveal robust structure features with only one run of the inversion even for an unrealistic reference model.

[19] The modified formulation is superior to the traditional two-step inversion in several respects. First, in the modified formulation, many period-by-period 2-D tomographic inversions in the first step and cell-by-cell 1-D S -velocity inversions in the second step are combined into a single formulation, dramatically reducing the computation time and reducing the number of intermediate inputs and outputs (in both inversion and forward procedures) and, consequently, facilitating synthetic tests and a posteriori model appraisals. Second, because the parameterized model $\Delta \beta_{ij}$ in equations (5) and (9) (or \mathbf{x} in equation (11)) is defined in three dimensions, it enables us to use the first-order gradient of the parameters in both the lateral direction and the vertical direction as 3-D smoothing constraints to construct a more physically reasonable model. In contrast, in the tradition two-step inversion it is not possible to apply lateral smoothing constraints in the second step because inversions are carried out separately, cell by cell.

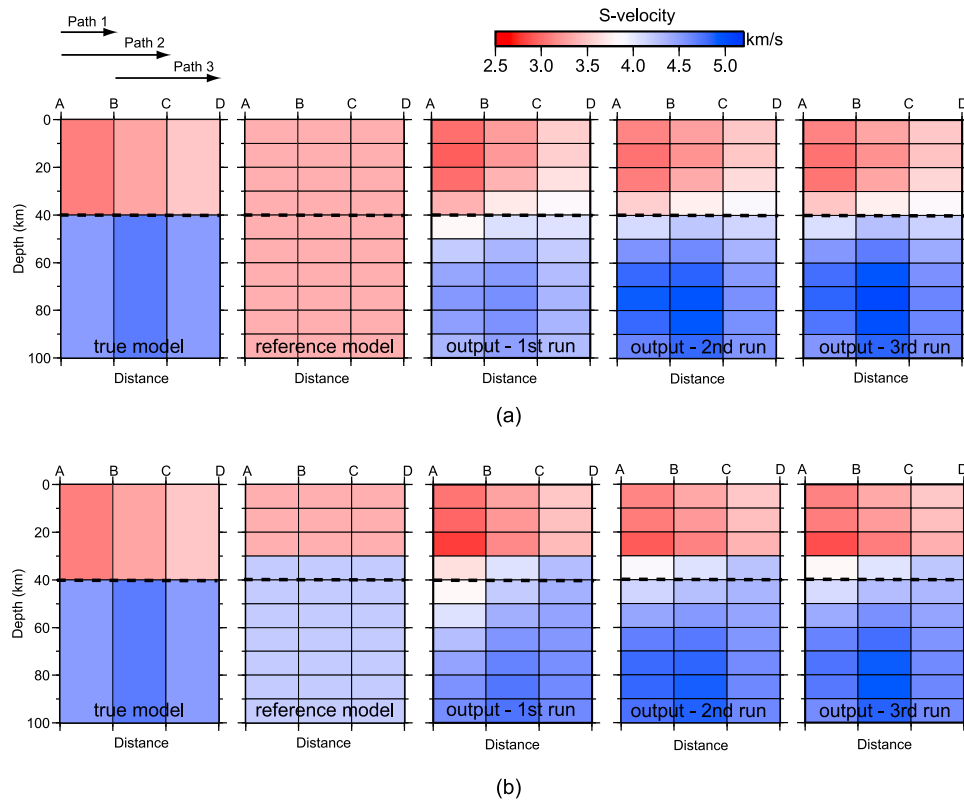


Figure 5. Results of synthetic tests performed to assess the validity of the surface-wave tomographic method used in the present study. Synthetic group velocities at periods of 5–140 s are set to three seismic rays, as shown at the upper left: path 1 (from A to B), path 2 (from A to C), and path 3 (from B to C). (a) The reference model is vertically and laterally homogeneous; (b) the reference model is laterally homogeneous, with two layers.

[20] We now apply the modified tomographic inversion method to a crustal and lithospheric study of China. Because the inclusion of observations of a greater number of periods would greatly enlarge the size of the sensitivity matrix \mathbf{G} , and considering the quantity of group-velocity measurements for each period, in the S -velocity model inversion we ultimately used group-velocity measurements at periods of 10–20 s with an interval of 2 s, at periods of 20–60 s with an interval of 5 s, and at periods of 60–180 s with an interval of 10 s. The 3-D model range is defined as 70°–150°E in longitude (x), 15°–60°N in latitude (y), and 0–600 km in depth (z). The 3-D model is parameterized with grid spacings of 1° in both longitude and latitude and with a variable layer thickness (from 5 to 50 km) in the z direction; the layer thickness is 5 km for depths less than 10 km, 10 km for depths from 10 to 300 km, and 50 km for depths from 300 to 600 km.

[21] We first performed a test using a 3-D S -velocity model as the reference model. The 3-D reference model was created by combining the interpolated S velocities of CRUST2.0 [Bassin *et al.*, 2000] for crustal structures and the S velocities of IASP91 [Kennett and Engdahl, 1991] for upper mantle structures. The data fits and inverted S -velocity model obtained using the 3-D reference model are similar to those obtained by inversion using the laterally homogeneous 1-D IASP91 as a reference model. Synthetic test results in Figures 5a and 5b have also shown that the inversion results

are not strongly related to the different choice of reference models. To better discriminate the structures constrained by real observational data and the structures inherited from the reference model, which is a direct way of evaluating the final model and the reliability of the inversion method, it is desirable to use a simple 1-D reference model rather than a complex 3-D reference model. We therefore ultimately chose using the laterally homogeneous IASP91 as the reference model. Because the Moho depths are not inverted, the inverted S velocities around the Moho are not analyzed because of the trade-off between Moho depth and S velocities around the Moho.

4. Model Appraisal

[22] To test both the efficiency and the reliability of the modified surface-wave tomography inversion method and the resolving power of the final model, here we give a brief description and discussion of model appraisal and checkboard tests undertaken for the China study.

[23] The fitting and root mean square (RMS) residuals between estimated and observed group velocities are important factors in evaluating the final inverted 3-D tomographic model [Feng *et al.*, 2007; Ritzwoller and Levshin, 1998; Vdovin *et al.*, 1999]. Figure 6a shows four dispersion fits between observed and estimated group velocities. Dispersions estimated from the inverted model

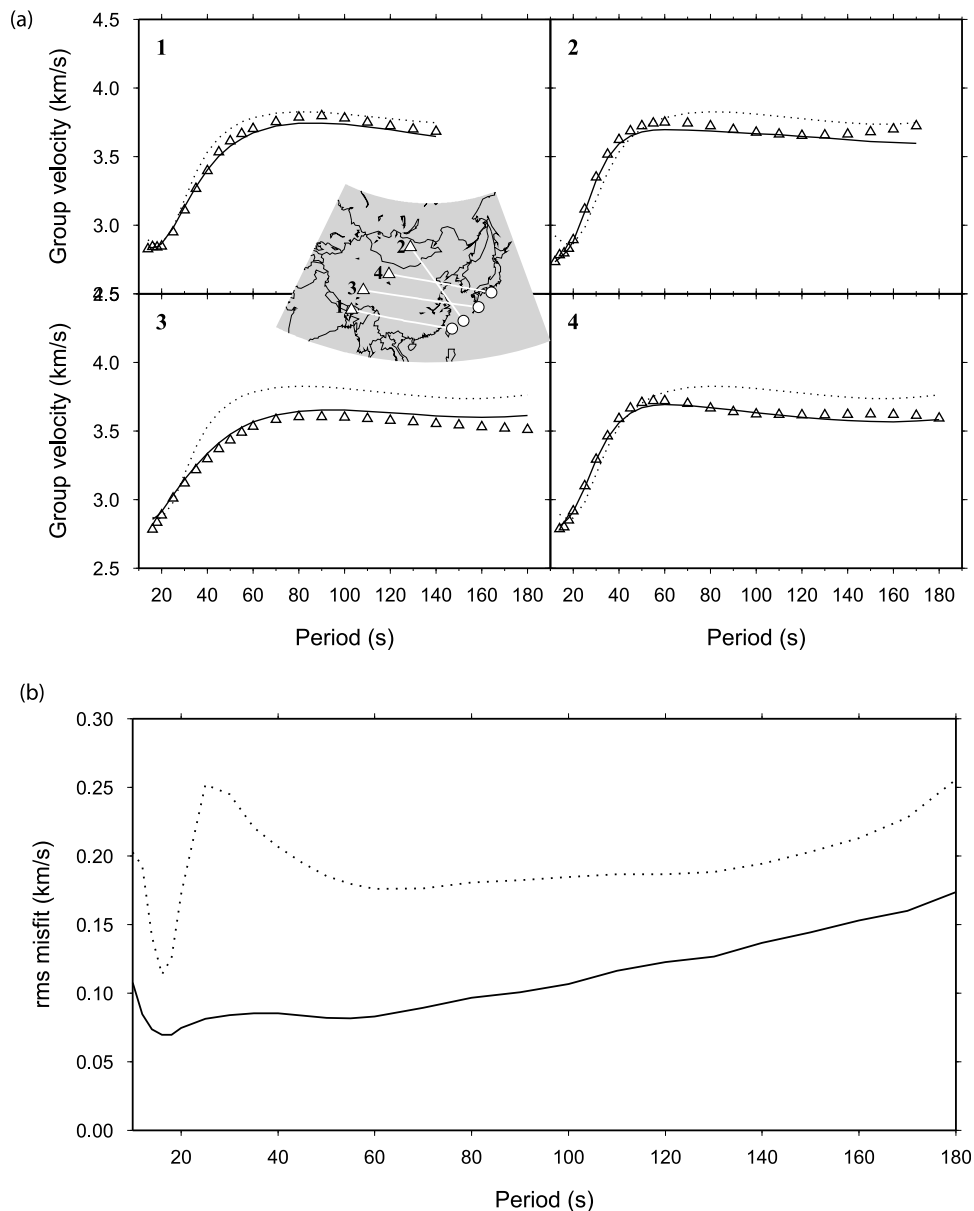
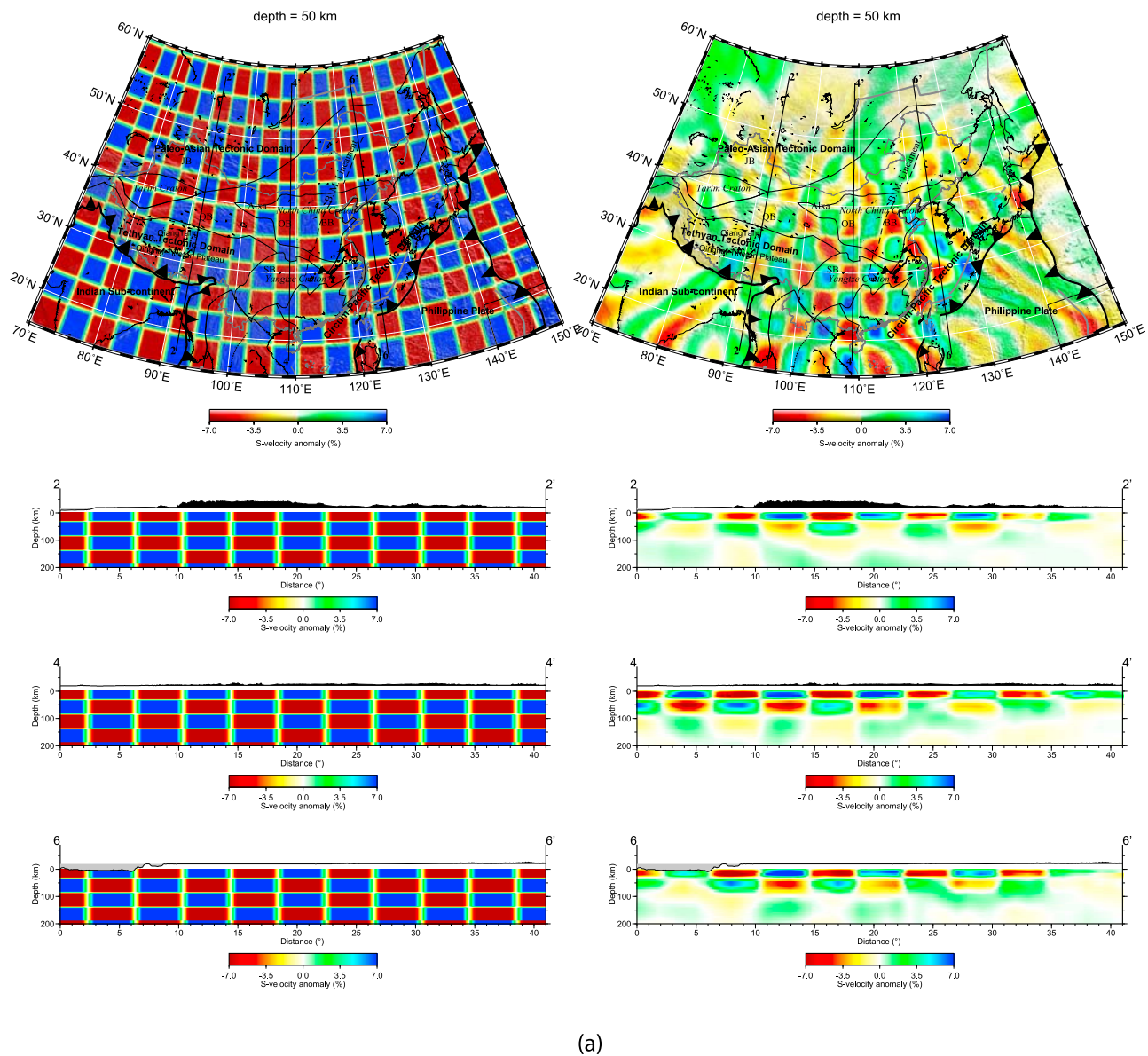


Figure 6. (a) Fits between four observed and predicted group-velocity dispersion curves. The dispersion number at the upper left in each graph corresponds to the raypath indicated by the same number in the inset map. Triangles denote observed dispersions, while solid and dotted lines represent predicted dispersions from the inverted *S*-velocity model and from the reference model, respectively. The inset map shows the paths, stations (triangles), and epicenters (circles) for the four dispersions. (b) Root mean square (rms) deviation between observed and predicted group velocities of the inverted (solid line) and reference models (dotted line).

(solid lines in Figure 6a) show a reasonable fit to the observed dispersions (triangles), better than the fits of the reference model (dotted lines). Figure 6b shows the total RMS misfit between observed and estimated regional group-velocity measurements. As expected, the group-velocity RMS misfit of the inverted model (solid line) is much smaller than that of the reference model (dotted line). In general, the inverted model produces an average $\sim 50\%$ reduction in RMS misfit relative to that of the reference model.

[24] Checkerboard tests are helpful in assessing the spatial resolving power of a tomographic model. To test lateral and vertical resolving power simultaneously, we set a 3-D synthetic model with horizontally and vertically alternating checkers. The input *S* velocities were set as varying by $\pm 7\%$ relative to the reference model. Because the surface wave of different periods has varying sensitivity and lateral resolution at different depths, we performed two synthetic tests with different checker sizes: one with a checker size of $4^\circ \times 4^\circ \times 5$ layers ($\sim 400 \times 444 \times 50$ km) in the *x*, *y*,



(a)

Figure 7. Lateral and vertical S -velocity slices of the checkerboard test results. The sizes of three-dimensional checkers are (a) $4^\circ \times 4^\circ \times 5$ layers (longitude and latitude 4° ; 5 layers vertically) and (b) $6^\circ \times 6^\circ \times 7$ layers. The left column shows slices of the input model, and the right column shows slices of the retrieved model. The locations of vertical cross sections are shown in the horizontal slices.

and z directions (4° in longitude and latitude and 5 layers in depth; Figure 7a) and the other with a checker size of $6^\circ \times 6^\circ \times 7$ layers ($\sim 600 \times 666 \times 70$ km; Figure 7b). Random noises were added to all the synthetic group-velocity measurements. The noise magnitude varied with period and was set as the average group-velocity RMS misfit of each period (solid line in Figure 6b).

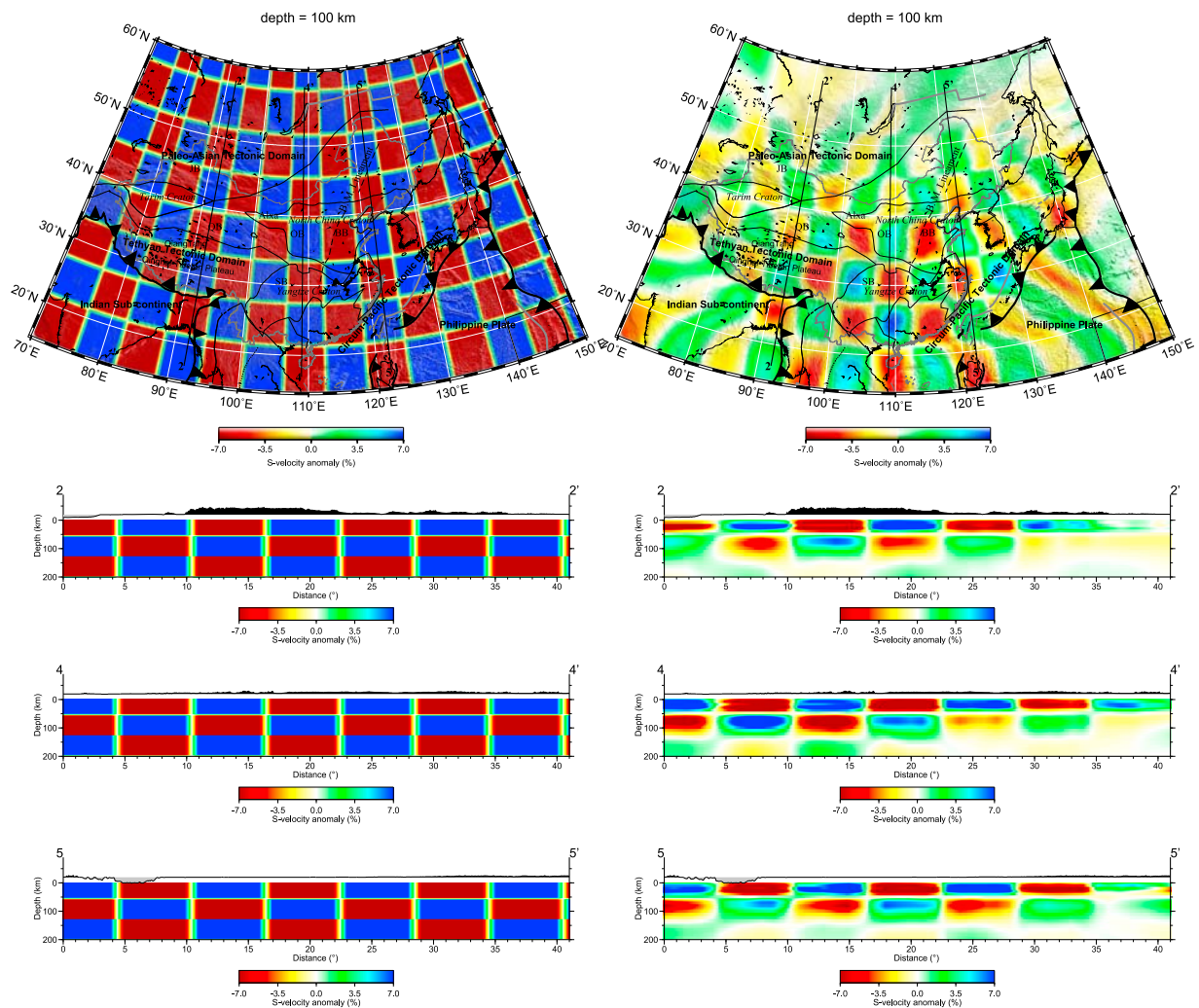
[25] Figure 7 shows the results of the horizontal and vertical checkerboard tests. For most of the Chinese mainland the model retrieved $4^\circ \times 4^\circ$ checkers down to a depth of 100 km and $6^\circ \times 6^\circ$ checkers down to a depth of 200 km. *Lebedev and Nolet* [2003] suggested that the actual resolution is half of the recovered checker size; therefore, the average lateral resolution length in the central part of our

study region is $\sim 2^\circ$ (~ 220 km) down to a depth of ~ 100 km and $\sim 3^\circ$ (~ 330 km) down to ~ 200 km; vertically, the average resolution is ~ 25 km down to a depth of ~ 100 km and ~ 35 km down to 200 km. The resolution decreases with depths and in marginal regions. Because a reliable lateral resolution of 3° extends down to a depth of ~ 200 km, we adopted a conservative approach and make interpretations only down to this depth.

5. Results

5.1. Horizontal Slices

[26] Our final S -velocity model is presented as perturbations (%) relative to the reference IASP91 model. The 3-D



(b)

Figure 7. (continued)

S -velocity model is first shown in the format of horizontal slices at four depths (5, 50, 100, and 150 km; Figure 8). Because the shortest period for our group-velocity data is 10 s, our data have resolving power for average information as shallow as to a depth ~ 10 km. Here the 5 km map (Figure 8a) represents the average S -velocity structures at a depth range of ~ 0 –10 km. Low velocities are associated with all of the major sedimentary basins in and around China, such as the intracontinental Tarim, Qaidam, Ordos, Sichuan, and Bohai Bay basins, and the back-arc basins east of the Chinese mainland. The strength of the low-velocity anomaly provides an indication of the sediment thickness. For example, the Tarim Basin, which contains a great thickness of sediments [Bassin *et al.*, 2000; Zhu *et al.*, 2006], produces a strong low-velocity anomaly.

[27] The thickness of the crust beneath China varies from ~ 30 km beneath eastern China to ~ 70 km beneath the Qinghai-Tibetan Plateau [Bassin *et al.*, 2000]. Consequently, the 50 km map (Figure 8b) shows the crustal

structure for the strongly elevated Qinghai-Tibetan Plateau and the uppermost mantle structure for other regions. Because the trade-off between S velocity and Moho depth may affect S -velocity structure around Moho depths, we do not consider structures between 30 and 70 km in depth. However, the occurrence of large-scale low velocities at a depth of 50 km (Figure 8b) beneath the Qinghai-Tibetan Plateau confirms the great thickness of the crust in this area; in comparison, at a 50 km depth in other parts of China, we observe high velocities of the uppermost mantle. The Tarim Basin shows weaker low velocities than does the Qinghai-Tibetan Plateau, suggesting a relatively thin crust. Weak low velocities are also observed beneath the island arcs of the Japan region and beneath the Indochina Peninsula.

[28] At a depth of 100 km (Figure 8c), high S velocities are considered to correspond to lithosphere, and low S velocities are considered to correspond to asthenosphere, because the thinnest lithosphere within the study area is ~ 80 km in eastern China. High velocities are widely imaged in most

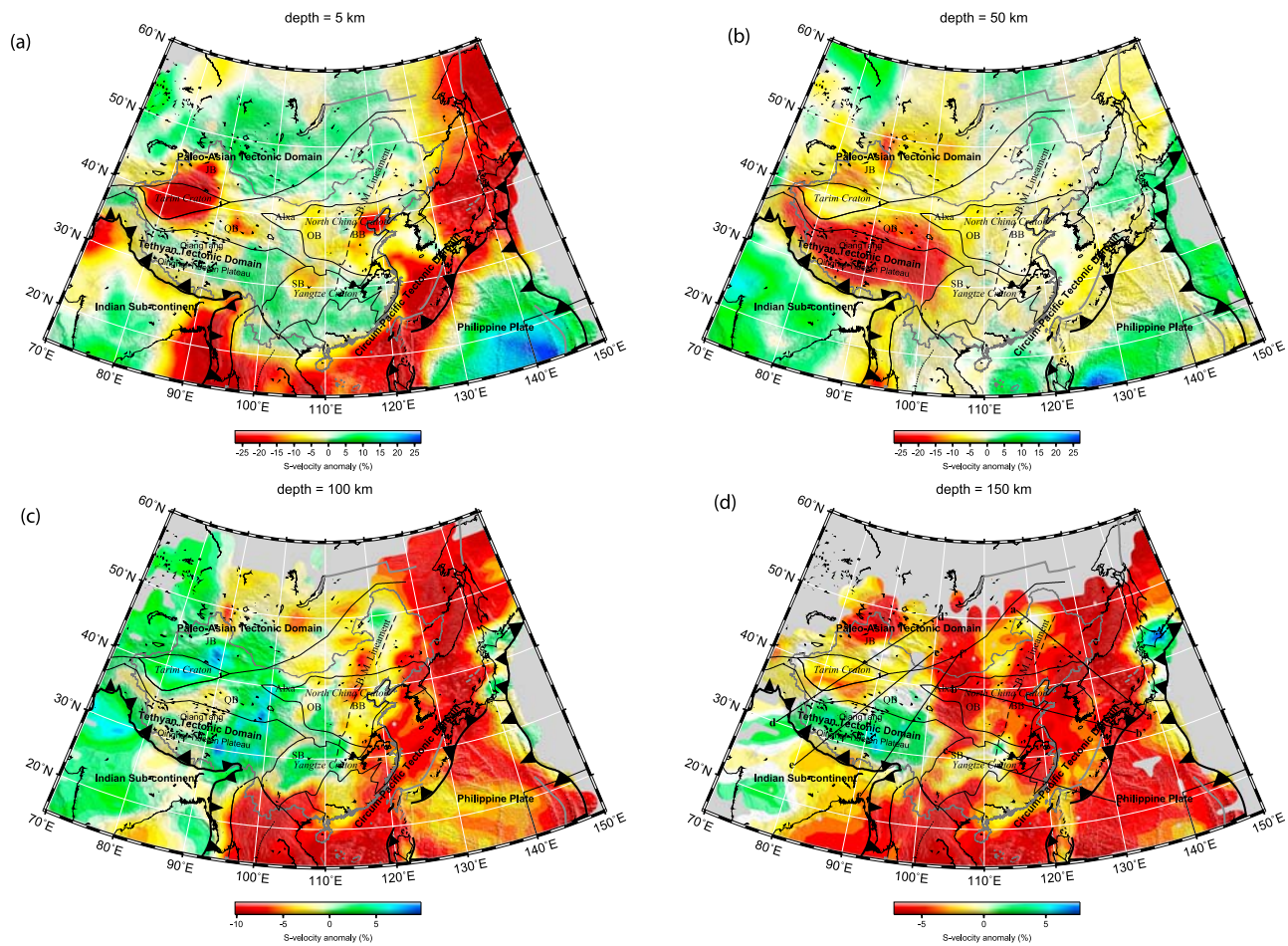


Figure 8. S -velocity model at depths of 5, 50, 100, and 150 km. The S -velocity anomaly is relative to IASP91. Areas with poor resolution are shown in gray. The 5 km map gives the average structure information above ~ 10 km.

cratonic areas, including the Tarim Craton, Junggar Basin, and Yangtze Craton, and beneath most of the Qinghai-Tibetan Plateau, except for the Qiangtang Terrane. High velocities of the Qinghai-Tibetan Plateau extend northeastward to the Alxa block in the westernmost NCC and eastward to the western Yangtze Craton.

[29] In contrast to other cratonic areas, the NCC shows strong east-west variations in velocity. The NCC can be subdivided, based on tectonic criteria, into three subblocks: the Ordos Basin in the west, the North China orogenic belt in the center, and the North China rift basins (e.g., Bohai Bay Basin) in the east [Jia and Zhang, 2005]. We consistently observed low velocities in the Alxa block and North China rift basins and high velocities in the Ordos Basin. This velocity pattern confirms the complex structure and evolution of the NCC.

[30] Another interesting high-velocity anomaly is observed in off-cratonic northeastern China. Low asthenospheric S velocities are mainly imaged in the Circum-Pacific tectonic domain in eastern and southern China. A north-south-trending low-velocity belt, running along approximately 105°E longitude, is imaged in the central part of the study region, starting from south of Baikal in the north, passing through the Alxa block, and ending west of the Yangtze Craton in the south. This low-velocity belt was also

imaged by Feng and An [2007] in their crustal model. The low-velocity belt is a crustal feature, as it overlaps the strong earthquake belt in central China [Zhang *et al.*, 2003]. Given that the low-velocity belt is also imaged at a 100 km depth in our model, the weak low-velocity zone may extend down to the lithosphere. This belt appears to separate the high velocities beneath the Qinghai-Tibetan Plateau and those beneath the Yangtze Craton and NCC.

[31] At a depth of 150 km (Figure 8d), high velocities are still found in the central Yangtze Craton and central Qinghai-Tibetan Plateau, indicating that the lithosphere extends down to a depth of at least 150 km in these areas. No high velocities are imaged beneath the NCC, suggesting a weak and thin lithosphere that does not reach a depth of 150 km, consistent with previous results [An and Shi, 2006; Huang *et al.*, 2003]. The high velocities in the Tarim Craton have also disappeared at this depth, which is inconsistent with the proposal of a stable and thick lithosphere for the Tarim, as derived from observations of surface heat flow [Wang, 2001]. Low velocities along the north-south belt in central China and in the Circum-Pacific tectonic domain in eastern and southern China remain the dominant anomalies at this depth, confirming that the north-south weak zone is not only a crustal but also a lithospheric feature.

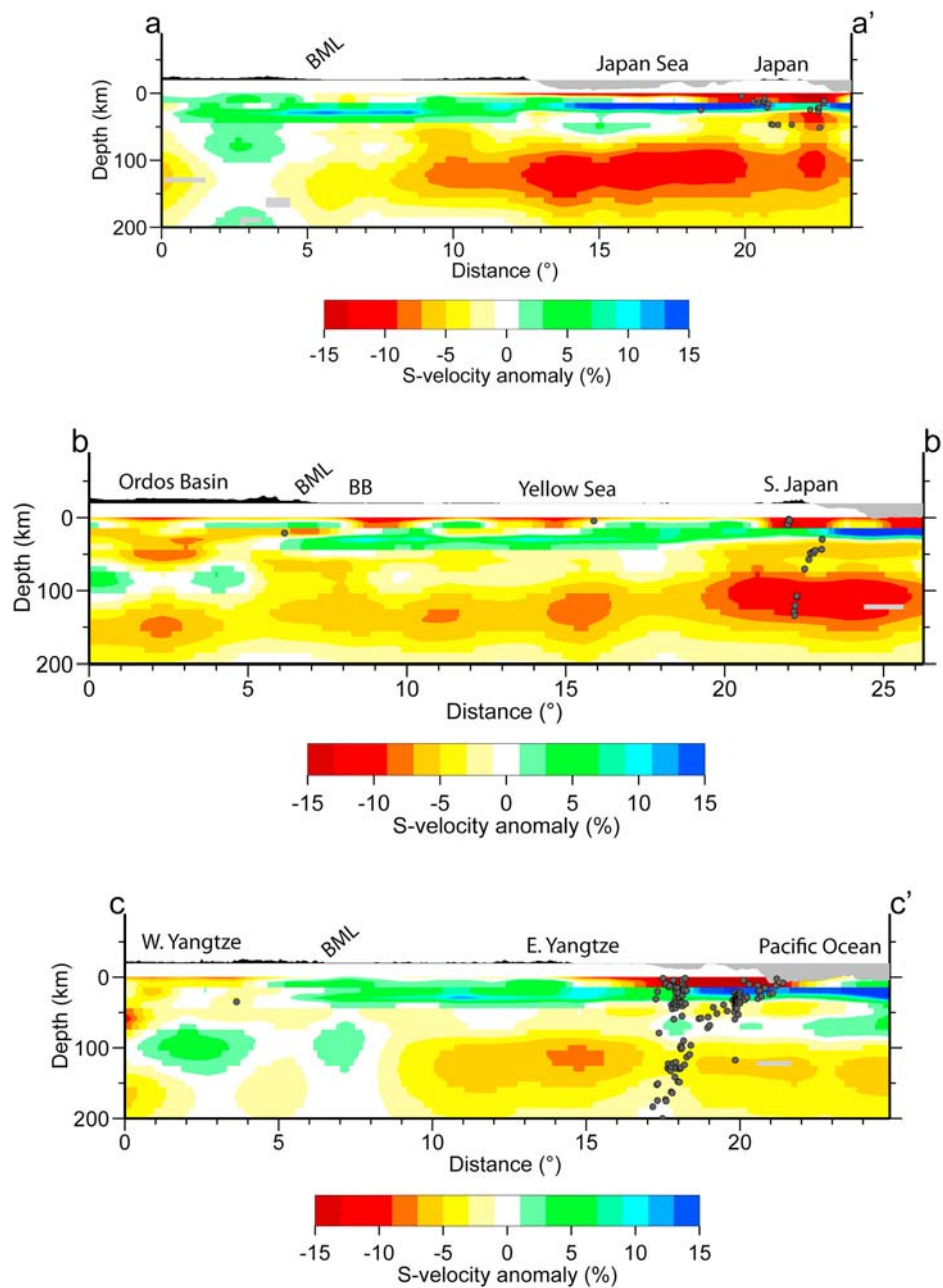


Figure 9. S -velocity model for different vertical cross sections. The S -velocity anomaly is relative to IASP91. Areas with poor resolution are shown in gray. BML, basin-mountain lineament; BB, Bohai Bay Basin.

5.2. Vertical Cross Sections

[32] Figure 9 shows six vertical cross sections across different regions of the final 3-D S -velocity model (locations of the cross sections are shown in Figure 8d). Above each profile the topography is illustrated with black shading for positive elevations (continent and islands) and gray shading for negative elevations (ocean). Historic earthquakes in the EHB catalog [Engdahl *et al.*, 1998] are also projected on each profile (dark gray circles).

[33] In Figure 9, profiles a-a', b-b', and c-c' mainly cross eastern China and the trench-arc zone east of China. A

number of common features are observed on these profiles. For example, low velocities are uniformly observed at depths of ~ 80 – 200 km in the eastern parts of the profiles, extending approximately from the trench-arc zone westward to the lineament that marks the basin-mountain transition (also referred to as the Daxin'anling-Taihangshan Lineament or North-South Gravity Lineament) in eastern China. West of the lineament, the three profiles show contrasting velocity features. For example, high velocities beneath northeastern China extend down to a ~ 200 km depth in the western part of profile a-a', to a depth of more than ~ 100 km beneath the Ordos Basin in the western part of profile b-b', and to a

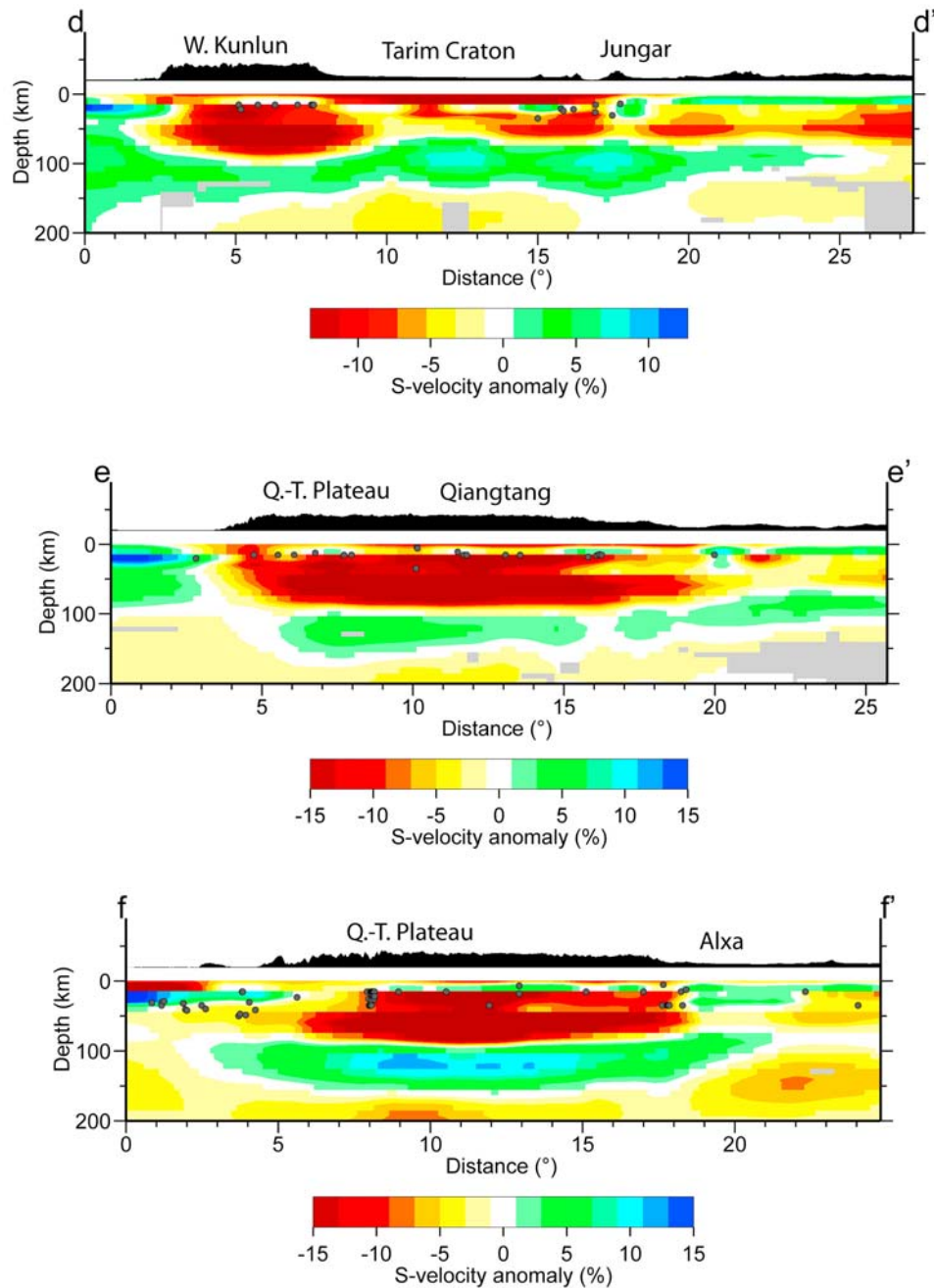


Figure 9. (continued)

~150 km depth beneath the Yangtze Craton in the western part of profile c-c'. The interesting high-velocity lithospheric anomaly beneath off-cratonic northeastern China requires further confirmation and discussion. In profile c-c' the western Yangtze Craton is characterized by high velocities, whereas the eastern craton shows low velocities.

[34] Intermediate and deep earthquakes are commonly found along the subducting Philippine Sea slab in the easternmost parts of profiles a-a', b-b', and c-c' in Figure 9, but only profile c-c', which crosses the western Philippine Sea Plate, shows the predicted normal to high velocities

along the earthquake belt. High velocities are not imaged in profiles a-a' and b-b', which cross the northwestern margin of the Philippine Sea Plate. Previous tomographic studies found that the northwestern subducting segment is characterized by localized high velocities surrounded by large areas of low velocities [e.g., *Abdelwahed and Zhao, 2007*], whereas the western segment is characterized by prominent high velocities [e.g., *Nakajima and Hasegawa, 2007*]. The absence of high velocities in profiles a-a' and b-b' in the present study possibly reflects the fact that the small high-

velocity anomaly is too small to be detected by our surface-wave tomography.

[35] Profiles d-d', e-e', and f-f' in Figure 9 mainly transect the Indian-Eurasian collision zone. Beneath the Qinghai-Tibetan Plateau, all three profiles show a very thick, low-velocity crust down to a depth of ~70 km and a deep, high-velocity lithosphere down to a depth of ~170 km. The elevated topography of the Qinghai-Tibetan Plateau corresponds well with the deepened lithosphere base (bottom of the high-velocity zone), which appears to be consistent with isostatic compensation. In profile d-d' high velocities beneath the Tarim Craton extend down to a depth of ~130 km, shallower than that beneath the western Kunlun to the south and shallower than that beneath the Junggar Basin to the north. These findings indicate that compared with the Qinghai-Tibetan Plateau, the Tarim Craton may be less deformed by the Indian-Eurasian collision and by the preceding Tethyan subduction. In profile e-e' a weak lithosphere is observed beneath the Qiangtang Terrane.

6. Discussion

[36] As described previously the NCC shows complex velocity variations and an extremely thin lithosphere compared with typical cratonic regions. The Qiangtang Terrane and the Tarim Craton have a lithosphere shallower and thinner than that in surrounding areas. A north-south-trending low-velocity belt extending down to at least 200 km is observed in central China, and low velocities are also observed in eastern and southern China. Here we consider the geodynamical mechanisms that produced the observed anomaly patterns.

6.1. Melting of the Subducting Slab and Lithospheric Thinning

[37] Deep earthquakes (>600 km depth) have been recorded beneath northeastern China, far from the nearest subduction zone. This indicates the existence of a deeply subducted slab at the transition between the lower and the upper mantle. Recent body-wave tomographic models [Fukao *et al.*, 2001; Huang and Zhao, 2006; Pysklywec and Ishii, 2005; van der Hilst *et al.*, 1997] have confirmed the existence of a deeply subducted slab beneath northeastern China, imaging a high-velocity slab extending from the surface (trench) to a depth of ~660 km, where it extends westward subhorizontally to northeastern China. The slab graveyard was imaged approximately beneath the NE-SW-trending lineament that marks the basin-mountain transition.

[38] In our model, low velocities that extend up to a depth of ~80 km are observed just above the subhorizontal subducting slab from arc islands (e.g., Japanese islands) in the east to the slab graveyard in the west (profile a-a' in Figure 9). The pattern of low velocities underlain by the high-velocity subhorizontal slab raises the possibility that the low velocities result from the ascent of hot partial melts derived from the slab. Such melts can erode the overlying lithosphere base, resulting in thinning of the lithosphere. If this erosion mechanism is valid, a similar velocity structure would be expected in other regions of the Circum-Pacific tectonic domain that are influenced by oceanic subduction. In fact, previous body-wave tomographic models [Fukao *et al.*, 2001; Huang and Zhao, 2006; Pysklywec and Ishii, 2005;

van der Hilst *et al.*, 1997] imaged a similar high-velocity subducting slab at the transition zone between the lower and the upper mantle beneath North China, and the slab graveyard was found beneath the central NCC (NE-SW-trending lineament).

[39] Low velocities in the asthenosphere are observed beneath eastern North China (profile b-b' in Figure 9), confirming the erosion effect of partial melts derived from the subducting slab on the overlying lithosphere structure. Prolonged erosion resulted in a remarkably thin lithosphere beneath the NCC. In addition, to the west of the Philippine Sea Plate in profile c-c', we observe low asthenospheric velocities beneath the eastern Yangtze Craton. The occurrence of a thinner lithosphere beneath the eastern Yangtze Craton than beneath the western Yangtze Craton (profile c-c') can also be interpreted to reflect the effect of erosion by partial melts.

6.2. Continental Collision and Lithospheric Extrusion

[40] In our model a double-thick lithosphere resulting from the Indian-Eurasian collision is widely imaged beneath the Qinghai-Tibetan Plateau, extending to the Qiangtang Terrane in the north and to approximately 105°E longitude in the east (see the slice at a 150 km depth in Figure 8d and profiles d-d', e-e', and f-f' in Figure 9). But why is the influence of the Indian-Eurasian collision bounded by the Qiangtang Terrane in the north and 105°E longitude in the east? Geographically, the Tarim Craton is located northwest of the Qiangtang Terrane, and the NCC and Yangtze Craton are located immediately east of 105°E longitude. Because cratonic areas (i.e., the Tarim Craton, NCC, and Yangtze Craton) are more stable and rigid than off-cratonic areas, the cratonic areas behaved as barriers during the Indian-Eurasian collision, thereby limiting the horizontal extent of the influence of the collision event. If this proposal is correct, the Qinghai-Tibetan Plateau would be subjected to compression, leading to elevation of the crust, thickening of the lithosphere, and extrusion of viscous materials along the rigid lithospheric boundaries of cratonic areas.

[41] Geodetic measurements [Lev *et al.*, 2006] indicate that surface displacements along the northeastern and southeastern margins of the Qinghai-Tibetan Plateau, relative to South China, are largely north-south, along the rigid western boundaries of the NCC and Yangtze Craton. SKS splitting analyses have demonstrated that the fast-wave directions in the upper mantle are similar to surface displacements along the northeastern [Liu *et al.*, 2001; Zhao *et al.*, 2007] and southeastern [Lev *et al.*, 2006; Sol *et al.*, 2007] margins of the plateau. The surface displacements and directions of fast waves in the upper mantle reveal the movement and flow directions of material under the influence of the Indian-Eurasian collision.

[42] The crustal dynamics of the eastern Tibetan Plateau are generally considered to involve the eastward flow of a low-viscosity (corresponding to low-velocity) lower-crustal layer, resulting in peripheral growth of the plateau or extrusion of the orogenic wedge (see the review by Harris [2007]). Because the similarity between crustal displacement and directions of fast waves in the upper mantle reflects the fact that the crust and upper mantle are subjected to similar boundary conditions [Holt, 2000], the extrusion

model for the crust is also applicable to the upper mantle. Accordingly, the north-south low-velocity belt in central China could be interpreted to reflect the extrusion of low-viscosity material from the Qinghai-Tibetan Plateau during the Indian-Eurasian collision. Possibly for the same reason, similarly low velocities are observed in the Qiangtang Terrane, which is bounded by the stable Tarim Craton.

7. Conclusions

[43] This study has applied the surface-wave tomographic method to a large number of regional and teleseismic fundamental-mode group-velocity measurements, yielding an improved 3-D *S*-velocity lithospheric model for China. On the basis of the results of checkerboard tests, the model has a lateral resolution of ~220 km down to a depth of 100 km and ~330 km down to 200 km in the central part of the study region and a vertical resolution of ~25 km down to a depth of 100 km depth and ~35 km down to 200 km. Sedimentary basins are imaged by low velocities in the upper crust. At a 100 km depth, high lithospheric velocities are observed in the Yangtze Craton and the Tarim Craton, and strong, low velocities in the asthenosphere are observed in the Circum-Pacific tectonic domain in eastern China, possibly indicating the partial melting of the subducting oceanic slab. In areas influenced by the Indian-Eurasian collision, a high-velocity anomaly is imaged beneath most of the Qinghai-Tibetan Plateau down to a depth of ~170 km but not beneath the Tarim Craton and the Qiangtang Terrane at a depth of 150 km. A north-south-trending low-velocity belt is imaged in both the crust and the upper mantle, along roughly 105°E longitude, in central China, possibly representing extrusion associated with the Indian-Eurasian collision.

[44] **Acknowledgments.** We thank the China Earthquake Data Center and DMC of IRIS for providing the seismic data. Douglas Wiens provided helpful suggestions that improved the manuscript. All figures (except for Figures 3 and 4) were prepared using the Generic Mapping Tools [Wessel and Smith, 1991]. This work was supported by the National Natural Science Foundation of China (NSFC-40504011 and NSFC-40674058) and the National Key Technology R&D Program (2006BAB18B08).

References

- Abdelwahed, M. F., and D. Zhao (2007), Deep structure of the Japan subduction zone, *Phys. Earth Planet. Inter.*, *162*, 32–52, doi:10.1016/j.pepi.2007.03.001.
- An, M., and M. S. Assumpção (2006), Crustal and upper mantle structure in intracratonic Paraná Basin, SE Brazil, from surface wave dispersion using genetic algorithm, *J. South Am. Earth Sci.*, *21*(3), 173–184, doi:10.1016/j.jsames.2006.03.001.
- An, M., and Y. Shi (2006), Lithospheric thickness of the Chinese continent, *Phys. Earth Planet. Inter.*, *159*, 257–266, doi:10.1016/j.pepi.2006.08.002.
- Artemieva, I. M., and W. D. Mooney (2001), Thermal thickness and evolution of Precambrian lithosphere: A global study, *J. Geophys. Res.*, *106*(B8), 16,387–16,414, doi:10.1029/2000JB900439.
- Bassin, C., G. Laske, and G. Masters (2000), The current limits of resolution for surface wave tomography in North America, *Eos Trans. AGU*, *81*, F897.
- Bijwaard, H., and W. Spakman (2000), Non-linear global P wave tomography by iterated linearized inversion, *Geophys. J. Int.*, *141*, 71–82, doi:10.1046/j.1365-246X.2000.00053.x.
- Bijwaard, H., W. Spakman, and E. R. Engdahl (1998), Closing the gap between regional and global travel time tomography, *J. Geophys. Res.*, *103*(B12), 30,055–30,078, doi:10.1029/98JB02467.
- Di Luccio, F., and M. E. Pasyanos (2007), Crustal and upper-mantle structure in the Eastern Mediterranean from the analysis of surface wave dispersion curves, *Geophys. J. Int.*, *169*(3), 1139–1152, doi:10.1111/j.1365-246X.2007.03332.x.
- Dziewonski, A. M., S. Bloch, and M. Landisman (1969), A technique for analysis of transient seismic signals, *Bull. Seismol. Soc. Am.*, *59*(1), 427–444.
- Engdahl, E. R., R. D. van der Hilst, and R. Buland (1998), Global teleseismic earthquake relocation with improved travel times and procedures for depth determination, *Bull. Seismol. Soc. Am.*, *88*, 722–743.
- Feng, C.-C., and T.-L. Teng (1983), Three-dimensional crust and upper mantle structure of the Eurasian continent, *J. Geophys. Res.*, *88*(B3), 2261–2272, doi:10.1029/JB088iB03p02261.
- Feng, M., and M. An (2007), Middle and upper crust shear-wave velocity structure of the Chinese mainland, *Acta Seismol. Sinica*, *20*(4), 359–369, doi:10.1007/s11589-007-0359-6.
- Feng, M., M. S. Assumpção, and S. van der Lee (2004), Group-velocity tomography and lithospheric *S*-velocity structure of the South American continent, *Phys. Earth Planet. Inter.*, *147*, 315–331, doi:10.1016/j.pepi.2004.07.008.
- Feng, M., S. Van der Lee, and M. Assumpção (2007), Upper mantle structure of South America from joint inversion of waveforms and fundamental-mode group velocities of Rayleigh waves, *J. Geophys. Res.*, *112*, B04312, doi:10.1029/2006JB004449.
- Friederich, W. (2003), The *S*-velocity structure of the East Asian mantle from inversion of shear and surface waveforms, *Geophys. J. Int.*, *153*, 88–102, doi:10.1046/j.1365-246X.2003.01869.x.
- Fukao, Y., S. Widiyantoro, and M. Obayashi (2001), Stagnant slabs in the upper and lower mantle transition region, *Rev. Geophys.*, *39*(3), 291–323, doi:10.1029/1999RG000068.
- Goes, S., and S. Van der Lee (2002), Thermal structure of the North American uppermost mantle inferred from seismic tomography, *J. Geophys. Res.*, *107*(B3), 2050, doi:10.1029/2000JB000049.
- Harris, N. (2007), Channel flow and the Himalayan-Tibetan orogen: A critical review, *J. Geol. Soc.*, *164*, 511–523, doi:10.1144/0016-76492006-133.
- He, Z.-q., Z.-f. Ding, T.-l. Ye, W.-g. Sun, and N.-l. Zhang (2002), Group velocity distribution of Rayleigh waves and crustal and upper mantle velocity structure of the Chinese mainland and its vicinity, *Acta Seismol. Sinica*, *15*(3), 269–275, doi:10.1007/s11589-002-0059-1.
- Herrmann, R. B. (1987), *Computer Programs in Seismology*, St. Louis Univ., St. Louis, Mo.
- Herrmann, R. B., and C. J. Ammon (2002), *Computer Programs in Seismology—Surface Waves, Receiver Functions and Crustal Structure*, St. Louis Univ., St. Louis, Mo.
- Holt, W. E. (2000), Correlated crust and mantle strain fields in Tibet, *Geology*, *28*(1), 67–70, doi:10.1130/0091-7613(2000)28<67:CCAMSF>2.0.CO;2.
- Huang, J., and D. Zhao (2006), High-resolution mantle tomography of China and surrounding regions, *J. Geophys. Res.*, *111*(B9), B09305, doi:10.1029/2005JB004066.
- Huang, Z., W. Su, Y. Peng, Y. Zheng, and H. Li (2003), Rayleigh wave tomography of China and adjacent regions, *J. Geophys. Res.*, *108*(B2), 2073, doi:10.1029/2001JB001696.
- Jia, S., and X. Zhang (2005), Crustal structure and comparison of different tectonic blocks in North China, *Chin. J. Geophys.*, *48*(3), 672–683.
- Kennett, B. L. N., and E. R. Engdahl (1991), Travel times for global earthquake location and phase identification, *Geophys. J. Int.*, *105*, 429–465, doi:10.1111/j.1365-246X.1991.tb06724.x.
- Lebedev, S., and G. Nolet (2003), Upper mantle beneath Southeast Asia from *S* velocity tomography, *J. Geophys. Res.*, *108*(B1), 2048, doi:10.1029/2000JB000073.
- Lev, E., M. D. Long, and R. D. van der Hilst (2006), Seismic anisotropy in eastern Tibet from shear wave splitting reveals changes in lithospheric deformation, *Earth Planet. Sci. Lett.*, *251*, 293–304, doi:10.1016/j.epsl.2006.09.018.
- Li, C., R. D. van der Hilst, and M. N. Toksoz (2006), Constraining P wave velocity variations in the upper mantle beneath Southeast Asia, *Phys. Earth Planet. Inter.*, *154*, 180–195, doi:10.1016/j.pepi.2005.09.008.
- Liu, F., K. Qu, H. Wu, Q. Li, J. Liu, and G. Hu (1989), Seismic tomography of the Chinese continent and adjacent region, *Chin. J. Geophys.*, *32*(3), 281–291.
- Liu, F.-T., H. Wu, J.-H. Liu, G. Hu, Q. Li, and K.-X. Qu (1991), 3-D velocity images beneath the Chinese continent and adjacent regions, *Geophys. J. Int.*, *101*, 379–394.
- Liu, X.-q., H.-l. Zhou, H. Li, and A.-d. Ji (2001), Anisotropy of the upper mantle in Chinese mainland and its vicinity, *Acta Seismol. Sinica*, *14*(4), 359–370, doi:10.1007/s11589-001-0114-3.
- Lomax, A., and R. Snieder (1995), The contrast in upper mantle shear-wave velocity between the East European Platform and tectonic Europe obtained with genetic algorithm inversion of Rayleigh-wave group dispersion, *Geophys. J. Int.*, *123*, 169–182, doi:10.1111/j.1365-246X.1995.tb06669.x.

- Martnez, M. D., X. Lana, J. Olarte, J. Badal, and J. A. Canas (2000), Inversion of Rayleigh wave phase and group velocities by simulated annealing, *Phys. Earth Planet. Inter.*, *122*(1–2), 3–17, doi:10.1016/S0031-9201(00)00183-7.
- Menzies, M., Y. Xu, H. Zhang, and W. Fan (2007), Integration of geology, geophysics and geochemistry: A key to understanding the North China Craton, *Lithos*, *96*, 1–21, doi:10.1016/j.lithos.2006.09.008.
- Nakajima, J., and A. Hasegawa (2007), Subduction of the Philippine Sea plate beneath southwestern Japan: Slab geometry and its relationship to arc magmatism, *J. Geophys. Res.*, *112*, B08306, doi:10.1029/2006JB004770.
- Paige, C. C., and M. A. Saunders (1982a), LSQR: An algorithm for sparse linear equations and sparse least squares, *Trans. Math. Software*, *8*(2), 43–71, doi:10.1145/355984.355989.
- Paige, C. C., and M. A. Saunders (1982b), Algorithm 583, LSQR: Sparse linear equations and least squares problems, *Trans. Math. Software*, *8*(2), 195–209, doi:10.1145/355993.356000.
- Pysklywec, R. N., and M. Ishii (2005), Time dependent subduction dynamics driven by the instability of stagnant slabs in the transition zone, *Phys. Earth Planet. Inter.*, *149*, 115–132, doi:10.1016/j.pepi.2004.08.019.
- Rapine, R., F. Tilmann, M. West, J. Ni, and A. Rodgers (2003), Crustal structure of northern and southern Tibet from surface wave dispersion analysis, *J. Geophys. Res.*, *108*(B2), 2120, doi:10.1029/2001JB000445.
- Ren, J., Z. Wang, B. Chen, C. Jiang, B. Niu, J. Li, G. Xie, Z. He, and Z. Liu (1999), *The Tectonics of China from a Global View—A Guide to the Tectonic Map of China and Adjacent Regions*, 32 pp., Geological Publishing House, Beijing.
- Ritzwoller, M. H., and A. L. Levshin (1998), Eurasian surface wave tomography: Group velocities, *J. Geophys. Res.*, *103*(B3), 4839–4878, doi:10.1029/97JB02622.
- Ritzwoller, M. H., N. M. Shapiro, M. P. Barmin, and A. L. Levshin (2002), Global surface wave diffraction tomography, *J. Geophys. Res.*, *107*(B12), 2335, doi:10.1029/2002JB001777.
- Schimmel, M., M. S. Assumpção, and J. C. VanDecar (2003), Seismic velocity anomalies beneath SE Brazil from P and S wave travel time inversions, *J. Geophys. Res.*, *108*(B4), 2191, doi:10.1029/2001JB000187.
- Shapiro, N. M., and M. H. Ritzwoller (2002), Monte Carlo inversion for a global shear-velocity model of the crust and upper mantle, *Geophys. J. Int.*, *151*, 88–105, doi:10.1046/j.1365-246X.2002.01742.x.
- Sieminski, A., J.-J. Lévesque, and E. Debayle (2004), Can finite-frequency effects be accounted for in ray theory surface wave tomography? *Geophys. Res. Lett.*, *31*, L24614, doi:10.1029/2004GL021402.
- Snoke, J. A., and D. E. James (1997), Lithospheric structure of the Chaco and Paraná basins of South America from surface-wave inversion, *J. Geophys. Res.*, *102*, 2939–2951, doi:10.1029/96JB03180.
- Snoke, J. A., and M. Sambridge (2002), Constraints on the S wave velocity structure in a continental shield from surface wave data: Comparing linearized least squares inversion and the direct search neighborhood algorithm, *J. Geophys. Res.*, *107*(B5), 2094, doi:10.1029/2001JB000498.
- Sol, S., et al. (2007), Geodynamics of the southeastern Tibetan Plateau from seismic anisotropy and geodesy, *Geology*, *35*(6), 563–566, doi:10.1130/G23408A.1.
- Song, Z., C. An, G. Chen, L. Chen, Z. Zhuang, Z. Fu, Z. Lu, and J. Hu (1994), 3D S-wave velocity structure of the crust and upper mantle, *Sci. China Ser. B*, *37*(1), 104–116.
- van der Hilst, R. D., S. Widiyantoro, and E. R. Engdahl (1997), Evidence for deep mantle circulation from global tomography, *Nature*, *386*, 578–584, doi:10.1038/386578a0.
- van der Voo, R., W. Spakman, and H. Bijwaard (1999), Tethyan subducted slabs under India, *Earth Planet. Sci. Lett.*, *171*, 7–20, doi:10.1016/S0012-821X(99)00131-4.
- Vdovin, O., J. A. Rial, A. L. Levshin, and M. H. Ritzwoller (1999), Group-velocity tomography of South America and the surrounding oceans, *Geophys. J. Int.*, *136*, 324–340, doi:10.1046/j.1365-246X.1999.00727.x.
- Villaseñor, A., M. H. Ritzwoller, A. L. Levshin, M. P. Barmin, E. R. Engdahl, W. Spakman, and J. Trampert (2001), Shear velocity structure of central Eurasia from inversion of surface wave velocities, *Phys. Earth Planet. Inter.*, *123*, 169–184, doi:10.1016/S0031-9201(00)00208-9.
- Wang, Y. (2001), Heat flow pattern and lateral variations of lithosphere strength in China mainland: Constraints on active deformation, *Phys. Earth Planet. Inter.*, *126*, 121–146, doi:10.1016/S0031-9201(01)00251-5.
- Wessel, P., and W. H. F. Smith (1991), Free software helps map and display data, *Eos Trans. AGU*, *72*, 411, doi:10.1029/90EO00319.
- Wu, F. T., and A. Levshin (1994), Surface-wave group velocity tomography of East Asia, *Phys. Earth Planet. Inter.*, *84*, 59–77, doi:10.1016/0031-9201(94)90034-5.
- Xia, J., R. D. Miller, and C. B. Park (1999), Estimation of near-surface shear-wave velocity by inversion of Rayleigh waves, *Geophysics*, *64*(3), 691–700, doi:10.1190/1.1444578.
- Yanovskaya, T. B., and V. M. Kozhevnikov (2003), 3D S-wave velocity pattern in the upper mantle beneath the continent of Asia from Rayleigh wave data, *Phys. Earth Planet. Inter.*, *138*, 263–278, doi:10.1016/S0031-9201(03)00154-7.
- Zhai, M., Q. Fan, H. Zhang, J. Sui, and J.-A. Shao (2007), Lower crustal processes leading to Mesozoic lithospheric thinning beneath eastern North China: Underplating, replacement and delamination, *Lithos*, *96*, 36–54, doi:10.1016/j.lithos.2006.09.016.
- Zhang, P., Q. Deng, G. Zhang, J. Ma, W. Gan, W. Min, F. Mao, and Q. Wang (2003), Active tectonic blocks and strong earthquakes in the continent of China, *Sci. China Ser. D*, *46* (Suppl. 2), 13–24.
- Zhang, Y.-S. (1998), Three-dimensional velocity structure beneath East Asia and its tectonic implication, in *Mantle Dynamics and Plate Interactions in East Asia*, edited by M. F. J. Flower, S.-L. Chung, C.-H. Lo, and T.-Y. Lee, pp. 11–23, AGU, Washington, D. C.
- Zhao, L., T. Zheng, L. Chen, and Q. Tang (2007), Shear wave splitting in eastern and central China: Implications for upper mantle deformation beneath continental margin, *Phys. Earth Planet. Inter.*, *162*, 73–84, doi:10.1016/j.pepi.2007.03.004.
- Zhu, J., J. Cao, X. Cai, Z. Yan, and X. Cao (2002), High resolution surface wave tomography in East Asia and West Pacific marginal seas, *Chin. J. Geophys.*, *45*(5), 679–698.
- Zhu, J., X. Cai, J. Cao, and Z. Yan (2006), Lithospheric structure and geodynamics in China and its adjacent areas, *Geol. China*, *33*(4), 793–802.
- Zomorodian, S. M. A., and O. Hunaidi (2006), Inversion of SASW dispersion curves based on maximum flexibility coefficients in the wave number domain, *Soil. Dyn. Earthquake Eng.*, *26*, 735–752, doi:10.1016/j.soildyn.2005.12.009.

M. An and M. Feng, MinZuDaXueNanLu 11, Institute of Geomechanics, Chinese Academy of Geological Sciences, Beijing 100081, China. (mei_feng_cn@yahoo.com.cn)